JACS Au
AN OPEN ACCESS JOURNAL OF THE AMERICAN CHEMICAL SOCIETY

pubs.acs.org/jacsau

Article

Structural and Spectroscopic Evidence for a Side-on Fe(III)−Superoxo Complex Featuring Discrete O−O Bond Distances

Hung-Ruei Pan, Hsin-Jou Chen, Zong-Han Wu, Pu Ge, Shengfa Ye,* Gene-Hsiang Lee, and Hua-Fen Hsu*

Cite This: *JACS Au* 2021, 1, 1389−1398

Read Online

ACCESS | Metrics & More | Article Recommendations | Supporting Information

ABSTRACT: The O−O bond length is often used as a structural indicator to determine the valence states of bound O_2 ligands in biological metal−dioxygen intermediates and related biomimetic complexes. Here, we report very distinct O−O bond lengths found for three crystallographic forms (1.229(4), 1.330(4), 1.387(2) Å at 100 K) of a side-on iron−dioxygen species. Despite their different O−O bond distances, all forms possess the same electronic structure of Fe(III)−$O_2^{\bullet-}$, as evidenced by their indistinguishable spectroscopic features. Density functional theory and ab initio calculations, which successfully reproduce spectroscopic parameters, predict a flat potential energy surface of an η^2-O_2 motif binding to the iron center regarding the O−O distance. Therefore, the discrete O−O bond lengths observed likely arise from differential intermolecular interactions in the second coordination sphere. The work suggests that the O−O distance is not a reliable benchmark to unequivocally identify the valence state of O_2 ligands for metal−dioxygen species in O_2-utilizing metalloproteins and synthetic complexes.

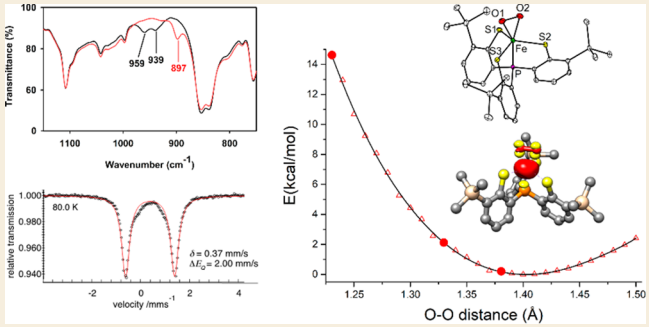

KEYWORDS: *iron−superoxo complex, superoxo, O_2 ligand, non-heme iron, intermediate*

INTRODUCTION

Reactive metal−dioxygen species, including metal−superoxide and −(hydro)peroxide, play important roles in various biological processes performed by O_2-utilizing metalloproteins.[1−4] The O−O bond length typically serves as an important indicator to identify the electronic state of these O_2-bound intermediates. For instance, free O_2, $O_2^{\bullet-}$, and O_2^{2-} have distinct O−O distances of 1.21, 1.33, and 1.49 Å, respectively.[5,6] Thus, based on the short O−O bond length of 1.23 Å, Cu^{I}−O_2 or Cu^{II}−$O_2^{\bullet-}$ were both considered in peptidylglycine-α-hydroxylating monooxygenase.[7] The structures of several iron-containing oxygenases featuring O−O bond lengths of 1.3−1.4 Å have been proposed as representatives of iron−superoxide complexes;[8−11] an O−O distance of 1.45 Å suggests an iron−peroxide species.[12] For nickel-containing quercetinase, the O−O bond length only can be refined to a range of 1.20−1.35 Å; therefore, the valency of the O_2 ligand cannot be unequivocally assigned.[13] Due to the low-resolution of X-ray structures of enzymes, geometric parameters obtained from well-defined synthetic analogues usually serve as references for comparison. Unfortunately, careful examination of individual categories of structurally characterized metal−superoxo or −peroxo complexes reveals that each has a wide range of O−O distances. Furthermore, abnormally short O−O distances have been attributed to librational motions of the diatomic O_2 ligand as signified by large thermal displacement parameters,[14,15] which can be mitigated by collecting the crystallographic data at low temperatures. Notably, even for X-ray crystallographic data of acceptable quality, the O−O bond length still varies over a wide range (Tables S1[14−21] and S2[16,22−51]). In particular, for metal−superoxo examples, an O−O bond distance of 1.231(6) Å was found for a Cr(III)−η^1-$O_2^{\bullet-}$ complex, but that of 1.383(2) Å was resolved for a Cu(II)−η^2-$O_2^{\bullet-}$ species.[15,17] Similarly, for metal−peroxo compounds, an O−O bond length of 1.361(5) Å was observed for a Co(III)−η^2-O_2^{2-} complex,[32] and that of 1.463(6) Å was obtained for [Fe^{III}(14-TMC)-(O_2)]$^+$ (TMC = tetramethyl cyclam).[25] A copper−dioxygen complex supported by a β-diketiminate ligand featuring an O−O bond length of 1.392(12) Å was initially proposed to be a Cu(III)−η^2-O_2^{2-} species,[22] but this formulation was later revised to Cu(II)−η^2-$O_2^{\bullet-}$ after re-evaluation using Cu K pre-edge X-ray absorption spectroscopy.[52] The correlation of O−O bond length and the valence state of bound O_2 ligands in metal−dioxygen complexes seems specious if not unclear. The

Received: April 25, 2021
Published: September 1, 2021

discrepancy in O−O bond lengths for O_2 ligands with the same valence state can be ascribed, at least in part, to dissimilarity in the geometry or coordination environment among complexes; therefore, solid evidence remains lacking.

In this work, we report a side-on iron−dioxygen complex, $[Fe(PS3'')(O_2)]^-$ (**1**) (PS3″ = $[P(C_6H_3\text{-}3\text{-}SiMe_3\text{-}2\text{-}S)_3]^{3-}$), showing various O−O bond lengths in different crystallographic forms where iron centers all possess similar geometry. However, the spectroscopic features of all forms are indistinguishable and conclude an electronic formulation of Fe(III)−$O_2^{\bullet-}$ species. All of our structural data are of excellent quality, and thermal displacement parameters of O atoms in the bound O_2 units are in an acceptable range, thus librational motion of the O_2 ligand is not a factor for their O−O distances. Instead, we propose that the subtle difference in crystal packing is likely responsible for the phenomena. This proposition is supported by the wave-function-based multireference calculations that predict a rather flat potential energy surface of side-on O_2 bonding to the Fe center with respect to the O−O distance.

RESULTS AND DISCUSSION

Synthesis, Characterization, and Reactivity of Complex 1

Reactions of trigonal-bipyramidal Fe(II) precursors, $[X][Fe(PS3'')(CH_3CN)]$ (PS3″ = $[P(C_6H_3\text{-}3\text{-}SiMe_3\text{-}2\text{-}S)_3]^{3-}$, X = PPh_4^+,[53] and $AsPh_4^+$; Figure S1 and Tables S3 and S4) with O_2 in CH_3CN at −20 °C or below generate a deep-blue solution with three intense bands at 504, 557, and 655 nm (Scheme 1 and Figure 1A). As monitored by UV−vis−NIR spectroscopy, this is a clean conversion with three isosbestic points at 400, 471, and 893 nm. The crystalline solids of the resulting species, complex **1**, were isolated by removing CH_3CN from the solution, followed by dissolving the residue in THF and hexane. The single crystals of [X][**1**]·2THF suitable for X-ray diffraction analyses were obtained by slow precipitation at −40 °C within several days. Complex **1** represents a rare example of structurally characterized non-heme Fe(III)-$O_2^{\bullet-}$ biomimetic complex, and the only other case is $[Fe^{III}(TAML)(O_2)]^{2-}$ (TAML is a tetraamido macrocyclic ligand), which is, however, generated by treating an Fe(III) precursor with KO_2.[16] Other synthetic Fe(III)−$O_2^{\bullet-}$ species have been only spectroscopically detected.[18,54−60]

Scheme 1. Formation of $[Fe(PS3'')(O_2)]^-$ (1) from the reaction of $[Fe(PS3'')(CH_3CN)]^-$ with O_2

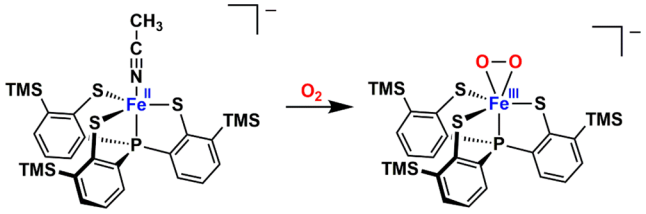

The molecular structures of [PPh_4][**1**]·2THF were determined by X-ray crystallography at 100, 150, and 200 K and that of [$AsPh_4$][**1**]·2THF at 100 K. Four sets of data are all of high quality without any detectable crystallographic disorder (Tables S5−S8). The geometry of all iron centers can be viewed as a pseudotrigonal-bipyramid formed by a PS3″ ligand and an η^2-O_2 moiety (Figure 2A,B and Figure S2). The average Fe−S distances (2.31−2.32 Å) in all structures are similar and are close to those reported for related trigonal-bipyramidal complexes, $[Fe^{III}(PS3'')L]^-$ (L = Cl^- and OCH_3^-), containing intermediate-spin Fe(III) centers.[61] However, the two independent molecules in a crystallographic asymmetric unit of the PPh_4^+ salt exhibit two distinguishable O−O distances irrespective of the temperature (tables in Figure 2A). Specifically, one with nearly identical Fe−O1 and Fe−O2 bond lengths displays an O1−O2 distance of 1.33−1.35 Å, and the other featuring a slightly asymmetrically coordinated O_2 motif possesses an O3−O4 length of 1.21−1.23 Å. In the structure of [$AsPh_4$][**1**], the η^2-O_2 ligand binds to the iron center symmetrically and has an O1−O2 distance of 1.387(2) Å (table in Figure 2B). The O−O bond distances observed for the symmetric Fe−O_2 unit in [PPh_4][**1**] and [$AsPh_4$][**1**] are in the longer end of the range (1.23−1.38 Å) found for all structurally characterized metal−superoxo complexes reported thus far (Table S1),[14−21] including $[Fe^{III}(TAML)(O_2)]^{2-}$ (1.323(3) and 1.306(7) Å).[16] It should be noted that $[Mn(PS3'')(O_2)]^-$, the Mn derivative of **1**, possesses an O−O distance of 1.379(3) Å but is formulated as a Mn(IV)−peroxo species.[40] In contrast, the O−O bond lengths determined for the asymmetric Fe−O_2 unit in [PPh_4][**1**] are in the shortest end of the range and are even close to that of free O_2 (1.21 Å). More importantly, the U_{eq} values for the two O atoms of the O_2 ligand fall into the reasonable range and only marginally increase with the temperature (Table S9). Thus, in the present case, such a large variation in the O−O distances cannot be simply rooted back to the librational motion of the O_2 ligand.

After scrutinizing all of the crystallographic data of [PPh_4][**1**] and [$AsPh_4$][**1**], we found subtle differences in

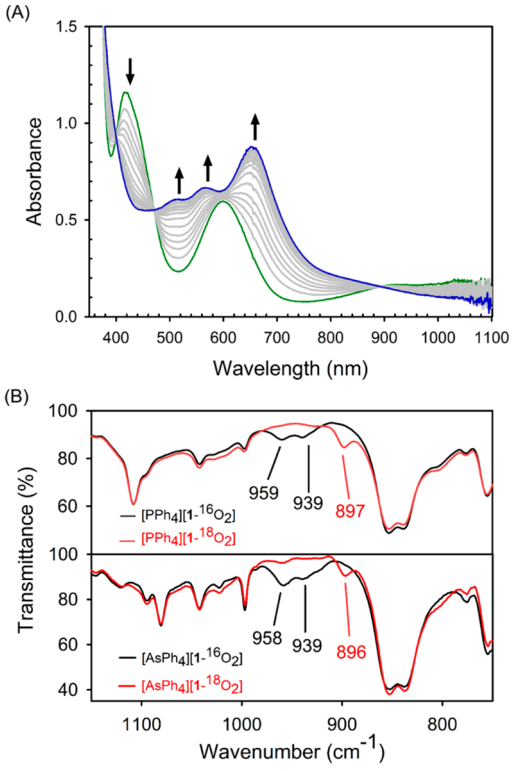

Figure 1. (A) Variation of the UV−vis−NIR spectrum of $[Fe(PS3'')(CH_3CN)]^-$ (green) reacting with O_2 to form **1** (blue) at −20 °C. (B) Infrared spectra of [PPh_4][**1**] and [$AsPh_4$][**1**] in KBr; $^{16}O_2$ sample (black) and $^{18}O_2$ sample (red).

https://doi.org/10.1021/jacsau.1c00184
JACS Au 2021, 1, 1389−1398

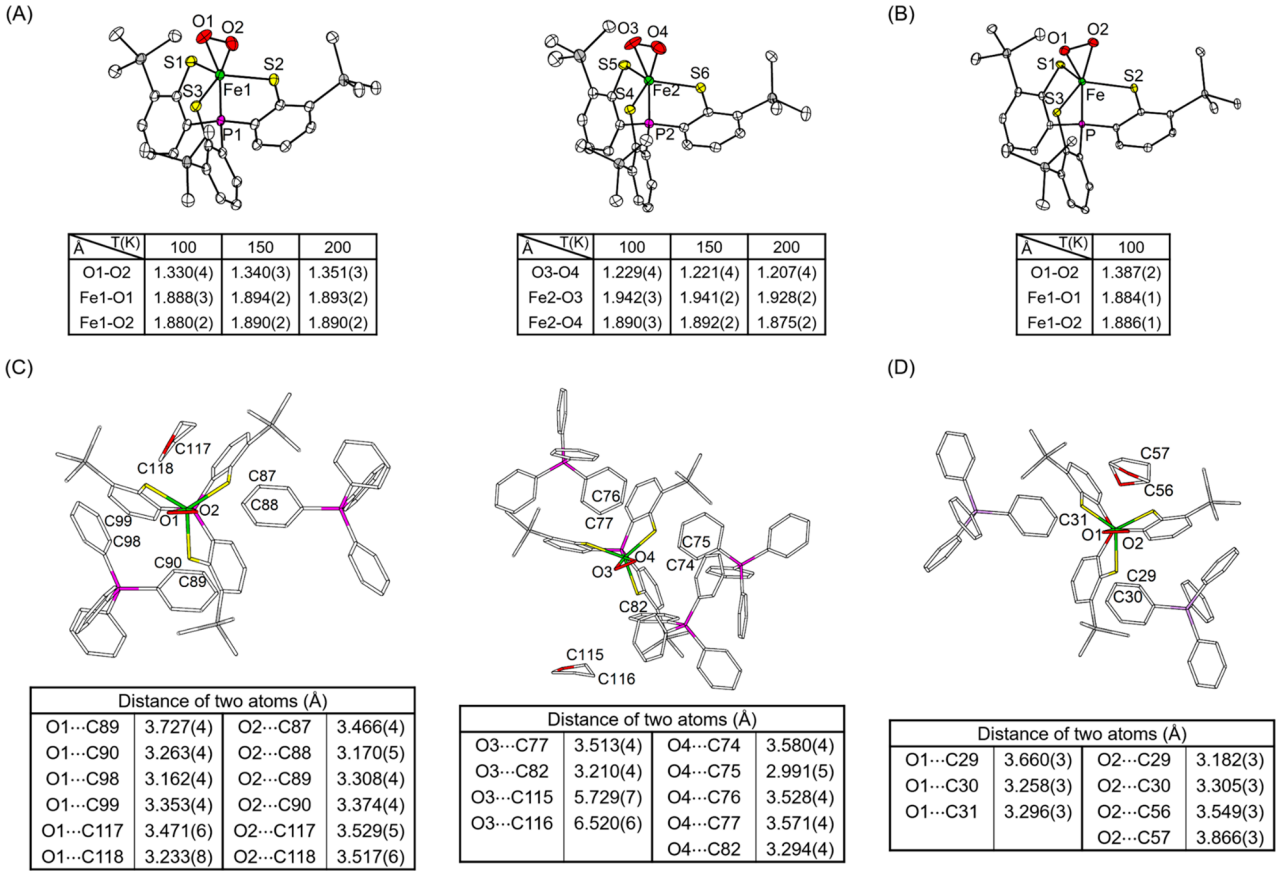

A \ T(K)	100	150	200
O1-O2	1.330(4)	1.340(3)	1.351(3)
Fe1-O1	1.888(3)	1.894(2)	1.893(2)
Fe1-O2	1.880(2)	1.890(2)	1.890(2)

A \ T(K)	100	150	200
O3-O4	1.229(4)	1.221(4)	1.207(4)
Fe2-O3	1.942(3)	1.941(2)	1.928(2)
Fe2-O4	1.890(3)	1.892(2)	1.875(2)

A \ T(K)	100
O1-O2	1.387(2)
Fe1-O1	1.884(1)
Fe1-O2	1.886(1)

Distance of two atoms (Å)			
O1···C89	3.727(4)	O2···C87	3.466(4)
O1···C90	3.263(4)	O2···C88	3.170(5)
O1···C98	3.162(4)	O2···C89	3.308(4)
O1···C99	3.353(4)	O2···C90	3.374(4)
O1···C117	3.471(6)	O2···C117	3.529(5)
O1···C118	3.233(8)	O2···C118	3.517(6)

Distance of two atoms (Å)			
O3···C77	3.513(4)	O4···C74	3.580(4)
O3···C82	3.210(4)	O4···C75	2.991(5)
O3···C115	5.729(7)	O4···C76	3.528(4)
O3···C116	6.520(6)	O4···C77	3.571(4)
		O4···C82	3.294(4)

Distance of two atoms (Å)			
O1···C29	3.660(3)	O2···C29	3.182(3)
O1···C30	3.258(3)	O2···C30	3.305(3)
O1···C31	3.296(3)	O2···C56	3.549(3)
		O2···C57	3.866(3)

Figure 2. ORTEP diagrams (35% probability) of (A) two independent molecules of $[PPh_4][\mathbf{1}]\cdot 2THF$ and (B) the molecule of $[AsPh_4][\mathbf{1}]\cdot 2THF$. The cations, solvated THF, and H atoms are omitted for clarity. The selected bond distances (Å) obtained at 100, 150, and 200 K for PPh_4^+ and 100 K for $AsPh_4^+$ salts are listed in the tables. (C) Two independent molecules of $[PPh_4][\mathbf{1}]\cdot 2THF$ and (D) the molecule of $[AsPh_4][\mathbf{1}]\cdot 2THF$ showing the neighboring groups of bound O_2 moieties. The selected distances between bound O_2 and neighboring C atoms of PPh_4^+ (or $AsPh_4^+$) and solvated THF are listed in the tables.

the second coordination sphere among three sets of the Fe−O_2 units (Figure 2C,D). The symmetrically bound O1−O2 moieties of $[PPh_4][\mathbf{1}]$ and $[AsPh_4][\mathbf{1}]$ are well surrounded by two phenyl rings of the countercation and a solvated THF molecule. Notably, the distances between both O atoms and a plethora of neighboring C atoms in these groups are 3.2−3.7 Å, implying the presence of a weak hydrogen bonding C−H···O network.[62] In contrast, the solvated THF molecule is further away from the bound O3−O4 ligand of $[PPh_4][\mathbf{1}]$ (O3···C115 = 5.729(7) Å and O3···C116 = 6.520(6) Å). In addition, only one side of the O3−O4 unit (nearby O4) is more tightly encircled with three phenyl rings of PPh_4^+ compared to the other side (nearby O3).

To elucidate the electronic structure origin for the distinct geometries of **1**, we carried out detailed spectroscopic characterizations. The KBr infrared (IR) spectrum of $[AsPh_4][\mathbf{1}]$ revealed a Fermi doublet at 958 and 939 cm^{-1}, which is shifted to 896 cm^{-1} upon ^{18}O substitution (Figure 1B). Therefore, this doublet should be attributed to the O−O stretch (ν_{O-O}) because the observed isotopic shift of 53 cm^{-1} is in excellent agreement with that (54 cm^{-1}) calculated for a diatomic O−O harmonic oscillator. Remarkably, although two different forms of **1** were found in the crystal structure of $[PPh_4][\mathbf{1}]$, its solid IR spectrum showed the same features as those for $[AsPh_4][\mathbf{1}]$ (Figure 1B). More importantly, a broad ν_{O-O} band at 958 cm^{-1}, which is shifted to 896 cm^{-1} for the ^{18}O-isotope-substituted sample, was identified in the IR spectrum of a THF solution of $[PPh_4][\mathbf{1}]$ (Figure S3). Compared to those reported for metal−superoxo complexes (1260−961 cm^{-1}) (Table S10), the ν_{O-O} frequencies measured for **1** are in the lower end. In line with this notion, a Badger's rule analysis of the O−O stretch at 950 cm^{-1} predicts a long O−O bond distance of 1.40 Å.[63] This value is substantially greater than that determined for the asymmetrically bound O_2 ligand of $[PPh_4][\mathbf{1}]$, although it is close to those for the symmetrically coordinated O_2 moiety of $[PPh_4][\mathbf{1}]$ and $[AsPh_4][\mathbf{1}]$. As elaborated elsewhere,[64] the bond-length/bond-strength correlations are just empirical relationships rather than physical laws, and due to various reasons, numerous exceptions have been reported already. Therefore, although the bound O_2 ligands in three crystallographic forms featured distinct O−O distances, they would have similar O−O force constants and stretching frequencies such that the low resolution of the measured IR spectra especially on solid samples failed to distinguish their differences.

Furthermore, both complexes possess well-isolated $S = 1$ ground states, as established by the temperature-dependent magnetic susceptibility measurements (Figures S4 and S5). The ^1H NMR spectra of both cation salts recorded at 223 K in THF-d_8 consistently displayed three peaks at the paramagnetic region, 14.56, −2.54, and −46.03 ppm, associated with the protons in the phenyl rings of the PS3″ ligand (Figure S6). These spectroscopic findings evidence that, despite having

https://doi.org/10.1021/jacsau.1c00184
JACS Au 2021, 1, 1389−1398

distinct O−O bond distances, all forms of **1** feature nearly identical electronic structure irrespective whether in a solid state or in solution.

The zero-field Mössbauer spectra of $[PPh_4][\mathbf{1}]$ and related PS3″ complex with varying Fe oxidation states are depicted in Figure 3. The isomer shift (δ) determined for **1** is comparable

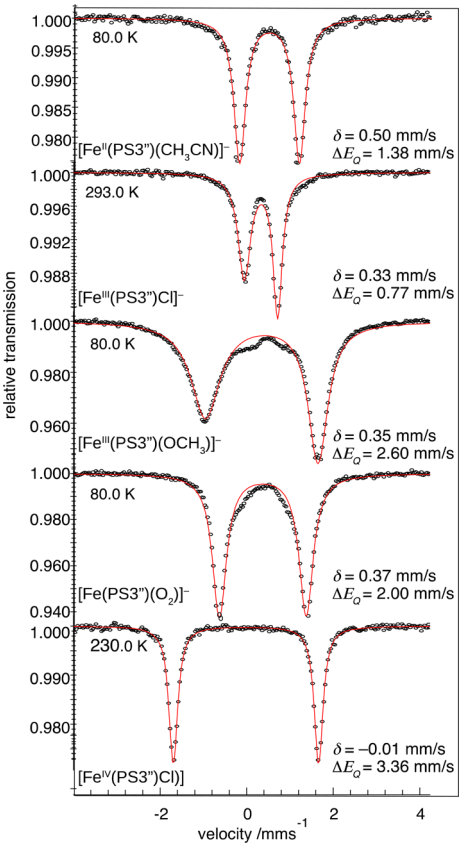

Figure 3. Zero-field Mössbauer spectra of **1** and related complexes measured at indicated temperatures. The asymmetric line shape found for $[Fe^{III}(PS3'')Cl]^-$ and $[Fe^{III}(PS3'')(OCH_3)]^-$ originates from not perfectly fast spin relaxation for half-integer spin systems. For details, see the Supporting Information, Figure S7).

to those found for intermediate-spin ferric species $[Fe^{III}(PS3'')Cl]^-$ and $[Fe^{III}(PS3'')(OCH_3)]^-$ but deviates by more than 0.1 mm/s from those for Fe(II) complex $[Fe^{II}(PS3'')(CH_3CN)]^-$ and Fe(IV) complex $[Fe^{IV}(PS3'')Cl]$. Therefore, Mössbauer data clearly indicate that **1** likely contains an intermediate-spin ferric center, as found for $[Fe^{III}(PS3'')Cl]^-$ and $[Fe^{III}(PS3'')(OCH_3)]^-$.[61] The different quadrupole splitting (ΔE_Q) measured for them can be attributed to their distinct coordination geometries.

Computational Studies on the Electronic Structure and the Potential Energy Surface of Complex 1

To gain in-depth insight into the electronic structure of **1**, density functional theory (DFT) calculations were undertaken. The quintet and septet states of **1** were estimated to lie 13.4 and 22.0 kcal/mol, respectively, above the triplet ground state. Furthermore, the B3LYP computed key metrics (Table S11) and spectroscopic parameters (ν_{O-O} = 1049 cm^{-1}, δ = 0.35 mm/s, and $|\Delta E_Q|$ = 2.26 mm/s) all match the experimental values within the uncertainty range of the calculations. In particular, considering that DFT computations often slightly overestimate O−O stretching frequencies, as exemplified by related Mn−superoxo and hydroperoxo complexes.[65,66] All findings thus lend credence to the computed electronic structure of **1** (Figure S8).

To further elucidate the bonding of complex **1**, we carried out wave-function-based multireference CASSCF(20,14) calculations on its S = 1 ground state. The active space comprises five Fe 3d based orbitals, O−O σ, σ^*, π_{ip}, π_{ip}^*, π_{op}, and π_{op}^* orbitals (ip = in the Fe−O−O plane, op = out of the Fe−O−O plane), the two Fe−S σ bonding orbitals (σ_{xy,x^2-y^2}) with respect to the interactions between Fe d_{xy,x^2-y^2} and the three equatorial S donors, and the P 3p centered bonding counterpart of the Fe d_{z^2} orbital (σ_{z^2}) (Figure 4A). As depicted in Figure 4B, the ground state wave function of **1** consists of two dominant electron configurations, viz., $(\sigma_{z^2})^2(\sigma_{xy})^2(\sigma_{x^2-y^2})^2(\pi_{op})^2(\pi_{op}^*)^2(\pi_{ip})^2(d_{yz})^2(d_{xz} + \pi_{ip}^*)^2(d_{xy})^1(d_{x^2-y^2})^1(d_{xz} - \pi_{ip}^*)^0(\sigma_{z^2}^*)^0(\sigma_{O-O}^*)^0$ (70%) and $(\sigma_{z^2})^2(\sigma_{xy})^2(\sigma_{x^2-y^2})^2(\pi_{op})^2(\pi_{op}^*)^2(\pi_{ip})^2(d_{yz})^2(d_{xz} + \pi_{ip}^*)^0(d_{xy})^1(d_{x^2-y^2})^1(d_{xz} - \pi_{ip}^*)^2(\sigma_{z^2}^*)^0(\sigma_{O-O}^*)^0$ (7%), where $d_{xz} + \pi_{ip}^*$ and $d_{xz} - \pi_{ip}^*$ denote the bonding and antibonding combinations derived from the interaction between Fe d_{xz} and O_2 π_{ip}^*. The latter configuration, in fact, corresponds to a double excitation from the bonding $d_{xz} + \pi_{ip}^*$ orbital to its antibonding $d_{xz} - \pi_{ip}^*$ one. Consequently, the occupation numbers of these two orbitals differ substantially from 2 and 0, respectively, as expected for a doubly occupied and a vacant orbital, but their sum (2.04) is very close to 2. As elaborated elsewhere, such an orbital occupation pattern signifies that **1** possesses considerable diradical character, which can be quantified by diradical index (d).[67,68] A value of d = 0% means that the two unpaired electrons interact so strongly that a covalent bond is formed, whereas the vanishing interaction between them is distinguished by d = 100%; consequently, 0% < d < 100% implies antiferromagnetic coupling between them with a hindered overlap. For complex **1**, d was computed to be 57%. This d value suggests that it contains an S = 3/2 ferric center that is strongly antiferromagnetically coupled to a superoxo radical, thereby yielding an overall triplet state. This electronic structure description is consistent with the sizeable negative spin population observed for the O_2 ligand (Figure 4C). By contrast, the negative spin population found for the anchor P atom stems from spin polarization of the fully occupied σ_{z^2} orbital induced by the unpaired electrons residing in the Fe d_{xy,x^2-y^2} orbitals.

To shed light on how the distinct O−O distance impacts the electronic structure of **1**, we performed a series of relaxed surface scans with the Perdew−Burke−Ernzerhof (PBE) density functional in which the O−O bond distance was systematically varied (Figures 5 and S9). On top of that, the electronic energy of each structure was further evaluated using the ab initio CASSCF(20,14)/NEVPT2 methods with the same active space discussed above. Theoretical results revealed that lengthening the O−O bond from 1.23 to 1.50 Å only causes a slight contraction of 0.07 Å for the average Fe−O_2 bond lengths (Figure 5A). More importantly, during this process, the bonding situation of **1** is nearly identical, as evidenced by the minute changes of the occupation numbers of the orbitals describing the dominant Fe−O_2 interaction, viz. $d_{xz} + \pi_{ip}^*$ and $d_{xz} - \pi_{ip}^*$ as well as O_2 σ and σ^* (Figure 5B,C and Figures S10 and S11). In support, the computed Mössbauer parameters based on the crystal structures are also in reasonable agreement with the experiment (Table S11). Consistent with such minimal electronic structure adjustments

https://doi.org/10.1021/jacsau.1c00184
JACS Au 2021, 1, 1389−1398

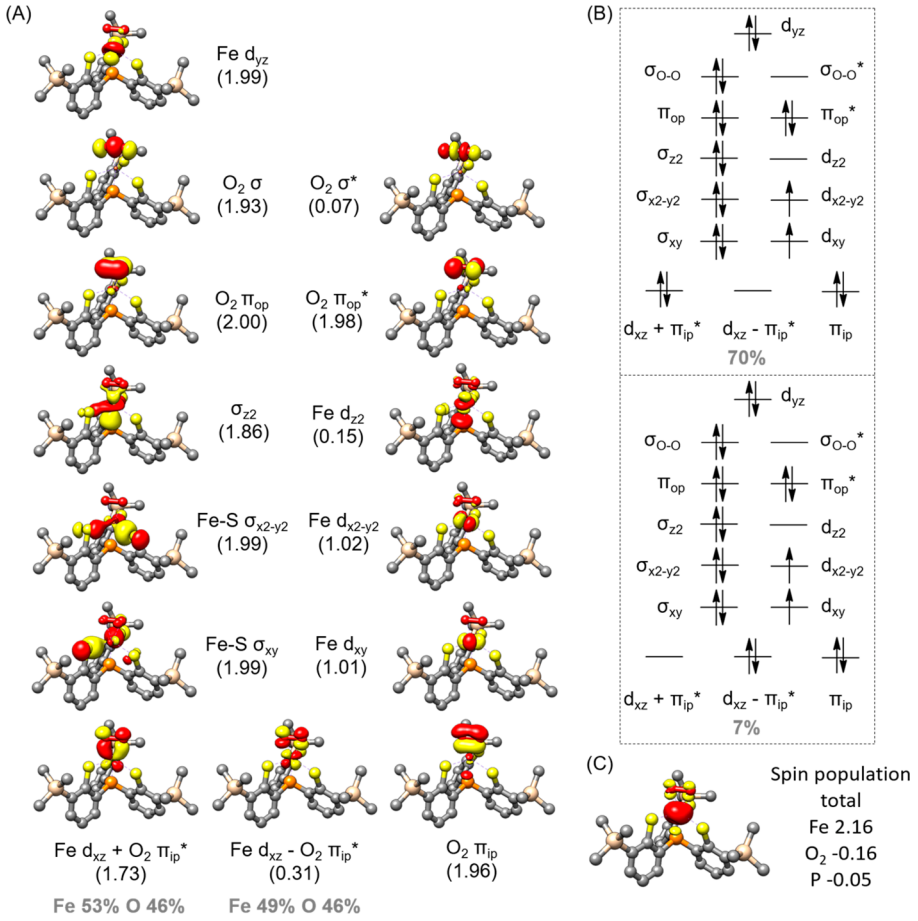

Figure 4. (A) Electronic structure of complex **1** with the O−O distance of 1.40 Å (the local minimum shown in Figure 5D) derived from CASSCF(20,14) calculations. Natural orbitals with occupation number in parentheses and contribution from atomic orbitals. (B) Two dominant electron configurations. (C) Spin density plot and important atomic spin population.

is that the energy variation is less than 6 kcal/mol for the O−O bond distance in the range of 1.29−1.50 Å (Figure 5D). However, upon shortening the O−O bond length from 1.28 to 1.23 Å, the energy difference increases from 6.8 to 14.6 kcal/mol. As shown in Figure S12, the CASSCF(20,14) computations without NEVPT2 corrections predict an even greater energy gap of 15.6 kcal/mol for the complex with an O−O bond distance of 1.23 Å relative to the minimum. These theoretical findings thus indicated that, due to lack of proper treatment of dynamic electron correlations, the present CASSCF(20,14)/NEVPT2 calculations still overestimate the energy separation of complex **1** with the slightly different O−O bond distance, especially for that less than 1.28 Å. To verify this notion, we also computed the energies of the three different forms found in the crystals (not shown in Figure 5). To do so, prior to ab initio calculations, only the positions of H atoms in the crystal structures were optimized while keeping those of the remaining atoms unchanged. The CASSCF-(20,14)/NEVPT2 computations delivered an energy gap as large as 22.7 kcal/mol for the form having a short O−O distance of 1.229 Å, although the other two with the O−O distances of 1.330 and 1.387 Å were found to lie 5.2 and 2.1 kcal/mol, respectively, above the minimum shown in Figure 5D. These results hence suggest that, to compute a more accurate potential energy surface (PES), a formidable active space consisting of more than 14 active orbitals has to be employed, which will be perused in our further study. Nevertheless, our theoretical findings unambiguously revealed that the side-on O_2 addition to the Fe center with respect to the varying O−O distance induces negligible electronic structure changes and hence likely has a rather flat PES. As a consequence, a subtle difference in weak interactions arising from the slightly different second coordination sphere likely affects their O−O distances considerably. This notion rationalizes why **1** exhibits three distinct O−O bond lengths in the crystals, but spectroscopic measurements cannot distinguish them. PBE calculations demonstrated that the end-on O_2 congener of **1** is destabilized by 4.8 kcal/mol relative the side-on one and features a considerably higher ν_{O-O} value (1151 cm^{-1}), which can be attributed to σ-type donation from the doubly occupied O_2 π_{ip}* to the empty Fe d_{z^2} orbital (Figure S13).

The reactivity of **1** exhibits an amphoteric nature, acting either as an electrophile or as a nucleophile. On one hand, its electrophilicity is demonstrated by its moderate capability of abstracting hydrogen atoms. Treatment of complex **1** with 2,6-di-*tert*-butylphenol (BDE_{O-H} = 82.8 kcal/mol) yields, primarily, 4,4′-dihydroxy-3,3′,5,5′-tetra-*tert*-butyldiphenyl as identified by electrospray ionization mass spectrometry (ESI-MS) measurements (Figure S14). The quantitative product analyses were performed by liquid chromatography (LC) and gave a yield of 88% (Figure S15). However, complex **1** fails to activate C−H bonds such as those in xanthene, 9,10-dihydroanthrene, and fluorene. On the other hand, complex

https://doi.org/10.1021/jacsau.1c00184
JACS Au 2021, 1, 1389−1398

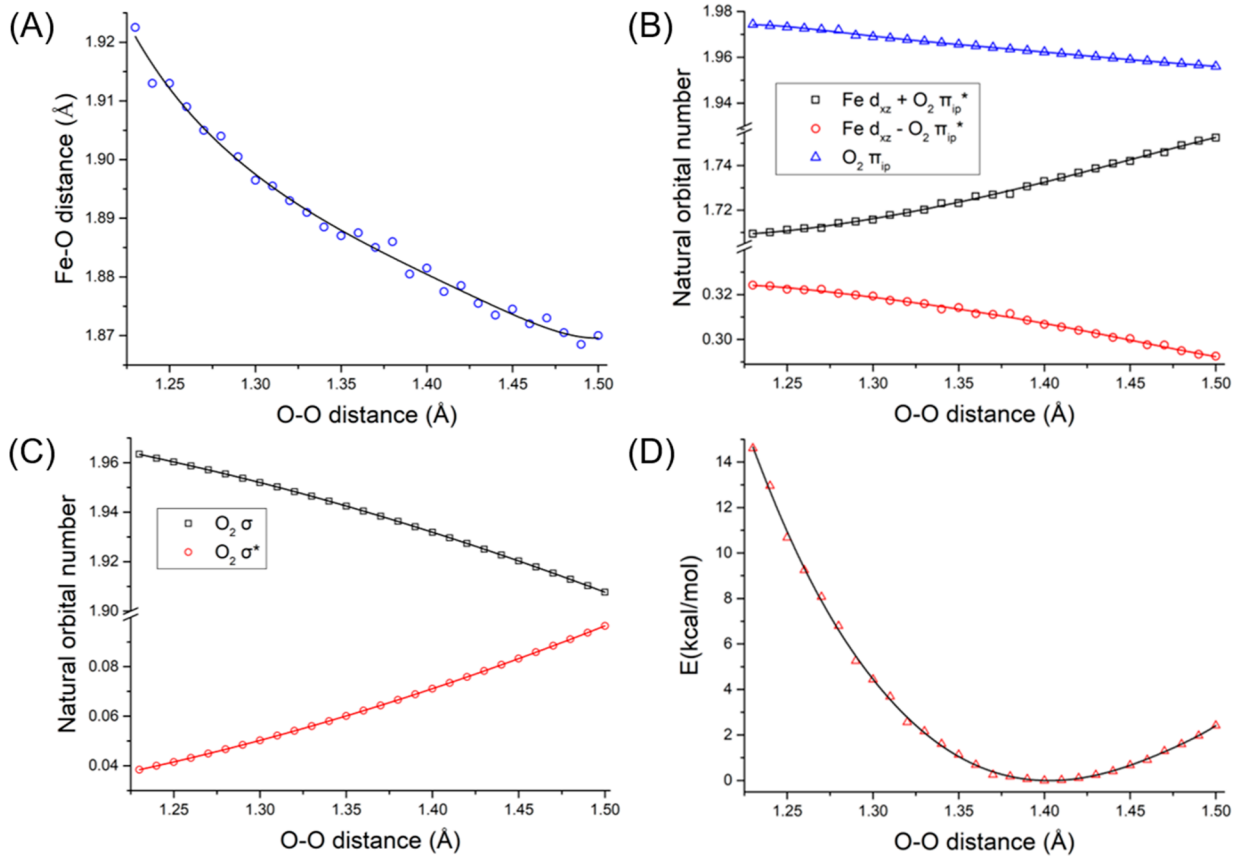

Figure 5. Average Fe−O_2 bond length (A), CASSCF(20,14)/NEVPT2 computed occupation−number variations of the d_{xz} + π_{ip}* and d_{xz} − π_{ip}* orbitals (B), those of O_2 σ and σ* orbitals (C), and computed energy change of **1** (D) as a function of the O−O bond distance.

1 can perform a nucleophilic oxidative reaction with benzaldehyde to furnish a dominant product of benzoate (detected by ESI-MS and quantified by LC, 95% yield, Figures S16 and S17). Kinetic measurements of complex **1** reacting with both substrates were taken by monitoring the disappearance of the characteristic band at 655 nm in UV−vis−NIR spectra (Figures S18 and S19). The obtained second-order rate constants (k_2) at 253 K were 1.61×10^{-4} and 3.86×10^{-4} M^{-1} s^{-1}, respectively (Figure S20).[69] Although the majority of reported Fe(III)−superoxo complexes were found to only exhibit electrophilic reactivity,[18,57,59,60] such an amphoteric behavior is also found for $[Fe(TAML)(O_2)]^{2-}$,[16] which further affirmed the notion that both complexes feature a similar electronic structure.

CONCLUSION

In summary, we have obtained a ferric−superoxo complex by addition of O_2 to an Fe(II) precursor bearing a tris(benzenethiolato)phosphine derivative. The X-ray structures revealed distinct O−O bond lengths in three different crystallographic forms, but they all shared the same spectroscopic features in the solid state and in solution. Consequently, their electronic structure is best described as an intermediate-spin ferric center antiferromagnetically coupled to a superoxo radical, giving an overall triplet state. The variation in O−O bond lengths across different crystallographic forms likely results from the subtle difference in the second coordination sphere environment of the side-on bound O_2 moiety because the computed PES of side-on O_2 bonding with respect to the O−O bond distance is rather flat. Thus, one should keep in mind that the assignment of valence states of O_2 moieties in metal−η^2-O_2 complexes simply using the O−O bond length alone is unsatisfactory. The overall implication provides a basis to question the electronic structure of metal−dioxygen intermediates when solely judged by the structural parameter of the O−O bond length.

EXPERIMENTAL SECTION

Materials and Methods

All experiments were carried out under dinitrogen with standard Schlenk techniques or N_2-filled glovebox. H_3[PS3″] (H_3[P(C_6H_3-3-Me_3Si-2-S)$_3$]) was synthesized according to the literature procedures.[70] [PPh_4][Fe(PS3″)Cl], [PPh_4][Fe(PS3″)(OCH_3)], and [Fe(PS3″)Cl] were prepared for Mössbauer measurements using synthetic protocols reported in the literature.[61,71] Solvents were dried and distilled by standard procedures. Otherwise, all starting materials were obtained commercially and used without further purification. The crystals were mounted on a glass fiber and quickly coated in epoxy resin. Diffraction measurements were performed with a Bruker SMART CCD diffractometer. The experimental temperature was controlled using an Oxford Cryosystems cooler. Least-squares refinement of the positional and anisotropic thermal parameters for the contribution of all non-hydrogen atoms and fixed hydrogen atoms was based on F^2. A SADABS absorption correction was made.[72] The SHELXTL structural refinement program was employed.[73] All non-hydrogen atoms were refined with anisotropic displacement factors. All hydrogen atoms were calculated using the riding model. UV−vis−NIR spectra were measured with a Hewlett-Packard 8453 spectrophotometer. ^{1}H NMR samples were characterized by a Bruker AMX500 spectrometer. A PerkinElmer Spectrum RX I spectrophotometer was used as the tool to record Fourier transform infrared spectroscopy. Elemental analysis data were measured with Elemetar

https://doi.org/10.1021/jacsau.1c00184
JACS Au 2021, 1, 1389−1398

vario EL III. ESI-MS spectra was performed by Q-Orbitrap MS. Product analysis for the reactivity was quantified by high-performance liquid chromatography (Agilent 1260 Infinity). Magnetic susceptibility data were measured from powder samples of solid material in the temperature range of 2−300 K using a SQUID susceptometer with a field of 0.1 T (MPMS-7, Quantum Design, calibrated with standard palladium reference sample, error <2%). Mössbauer spectra were recorded on conventional spectrometers with alternating constant acceleration of the γ source. The minimum experimental line width was 0.24 mm/s (full width at half-height). The sample temperature was maintained constant in an Oxford Instruments Variox cryostat. Isomer shifts are quoted relative to iron metal at 300 K. The zero-field spectra were simulated with Lorentzian doublets with the program *mf.SL* developed by Dr. Eckhard Bill at the Max-Planck Institute for Chemical Energy Conversion. Kinetic studies of complex **1** reacting with 2,6-DTBP and benzaldehyde were performed. Different equivalents of substrates were reacted with complex **1** (0.2 mM) in THF at −20 °C. The reactions were monitored by UV−vis−NIR spectroscopy with the disappearance of the characteristic band at 655 nm. The pseudo-first-order rate constants (k_{obs}) increase linearly as a function of the substrate concentration, giving second-order rate constants. The product analyses were quantified by LC. The product yield was compared against the standard curves with authentic samples.[74] Benzil and phenol were used as internal standards for the reactions with 2,6-di-*tert*-butylphenol and benzaldehyde, respectively.

Synthesis of $[AsPh_4][Fe(PS3'')(CH_3CN)]\cdot 5CH_3CN$

H_3PS3'' (0.1000 g, 0.174 mmol) and Li (0.0037 g, 0.522 mmol) were dissolved in CH_3OH to generate a pale yellow solution. After $FeCl_2$ (0.0221g, 0.174 mmol) was added to the reaction mixture, the solution color changed to emerald immediately. The solvent was removed, and the residue was dissolved in CH_3CN. After $AsPh_4Cl\cdot H_2O$ was added, the solution was stored at −40 °C. The dark green crystals of $[AsPh_4][Fe(PS3'')(CH_3CN)]\cdot 5CH_3CN$ were produced after 1−2 days. Yield: 63.1%. Electronic absorption in CH_3CN (λ, nm; ε, M^{-1} cm^{-1}): 417 (4.48×10^3); 601, (2.33×10^3). Anal. Calcd for $C_{53}H_{59}AsFeNPS_3Si_3$ ($[AsPh_4][Fe(PS3'')(CH_3CN)]$): C, 60.50; H, 5.65; N, 1.33; S, 9.14. Found: C, 60.37; H, 5.82; N, 1.37; S, 9.07.

Synthesis of $[PPh_4][Fe(PS3'')(^{16/18}O_2)]\cdot 2THF$ ($[PPh_4][1]\cdot 2THF$)

Adding O_2 into $[PPh_4][Fe(PS3'')(CH_3CN)]$ (0.005 g, 5×10^{-3} mmol) in CH_3CN at −40 °C generated a blue solution. The solvent was removed, and the residue was recrystallized from THF/hexane at −40 °C to give a dark blue crystalline solid of $[PPh_4][\mathbf{1}]\cdot 2THF$ in a quantitative yield. Electronic absorption in THF (λ, nm; ε, M^{-1} cm^{-1}): 504 (1.88×10^3); 557 (1.99×10^3); 655 (2.59×10^3). Anal. Calcd for $C_{51}H_{56}FeO_2P_2S_3Si_3$ ($[PPh_4][\mathbf{1}]$): C, 61.30; H, 5.65; S, 9.63. Found: C, 60.51; H, 5.98; S, 9.28. IR (KBr, ν, cm^{-1}): 959, 939 ($^{16}O-^{16}O$); 897 ($^{18}O-^{18}O$).

Synthesis of $[AsPh_4][Fe(PS3'')(^{16/18}O_2)]\cdot 2THF$ ($[AsPh_4][1]\cdot 2THF$)

Adding O_2 into $[AsPh_4][Fe(PS3'')(CH_3CN)]$ (0.005 g, 4.7×10^{-3} mmol) in CH_3CN at −40 °C generated a blue solution. The solvent was removed, and the residue was recrystallized from THF/hexane at −40 °C to give a dark blue crystalline solid of $[AsPh_4][\mathbf{1}]\cdot 2THF$ in a quantitative yield. Electronic absorption in THF (λ, nm; ε, M^{-1} cm^{-1}): 504 (2.634×10^3); 557 (2.701×10^3); 655 (3.407×10^3). Anal. Calcd for $C_{55}H_{64}AsFeO_3PS_3Si_3$ ($[AsPh_4][\mathbf{1}]\cdot THF$): C, 59.23; H, 5.78; S, 8.63. Found: C, 58.19; H, 5.706; S, 8.805. IR (KBr, ν, cm^{-1}): 958, 939 ($^{16}O-^{16}O$); 896 ($^{18}O-^{18}O$).

Computational Setup

Geometry optimizations were performed with the PBE[75] and B3LYP[76,77] density functionals, and the RI[78] and RIJCOSX[79] approximations were used to accelerate the calculations, respectively. The def2-TZVP for the first coordination sphere and def2-SVP basis sets[80] for the remaining atoms were applied in combination with the auxiliary basis sets def2/J.[81] As shown in Table S11, the estimated geometric metrics using both density functionals are in reasonable agreement with experiment (for details, see the Supporting Information). In line with this finding, the computed electronic structures are nearly identical. However, the B3LYP calculations predicted that **1** with a side-on O_2 moiety lies above its corresponding isomer with an end-on O_2 motif by 9.5 kcal/mol, whereas the PBE calculations suggested that the latter is destabilized by 4.8 kcal/mol. Therefore, relaxed scans of the O−O bond distance were carried out using the PBE density functional only. The Mössbauer spectroscopic parameters were computed using the B3LYP density functional. The CP(PPP)[82] basis set for Fe was employed, and the def2-TZVP[83] basis set for O, P, and S and the def2-SV(P) basis set[84] for remaining atoms were used.

Isomer shifts δ were calculated from the electron densities r_0 at the Fe nuclei by employing the linear regression:

$$\delta = \alpha\cdot(\rho_0 - C) + \rho$$

Here, C is a prefixed value, and α and β are the fit parameters. Their values for different combinations of the density functionals and basis sets can be found in our earlier work ($\alpha = -0.366$, $\beta = 2.852$, $C = 111810$).[85,86]

Quadrupole splittings, ΔE_Q, were obtained from electric field gradients V_{ij} ($i = x, y, z$; V_{ii} are the eigenvalues of the electric field gradient tensor) using a nuclear quadrupole moment $Q(^{57}Fe) = 0.16$ barn:[87]

$$\Delta E_Q = \frac{1}{2}eQ\cdot V_{zz}\cdot\sqrt{1 + \frac{1}{3}\eta^2}$$

Here, $\eta = \frac{V_{xx} - V_{yy}}{V_{zz}}$ is the asymmetry parameter.

All calculations were performed by using the ORCA quantum chemical program package.[88]

■ ASSOCIATED CONTENT

Supporting Information

The Supporting Information is available free of charge at https://pubs.acs.org/doi/10.1021/jacsau.1c00184.

Crystallographic data for $[AsPh_4][\mathbf{1}]$ (CIF)
Crystallographic data for $[PPh_4][\mathbf{1}]$ at 100 K (CIF)
Crystallographic data for $[PPh_4][\mathbf{1}]$ at 150 K (CIF)
Crystallographic data for $[PPh_4][\mathbf{1}]$ at 200 K (CIF)
Crystallographic data for $[AsPh_4][Fe(PS3'')(CH_3CN)]$ (CIF)
ORTEP diagrams, NMR spectra, data tables (PDF)

■ AUTHOR INFORMATION

Corresponding Authors

Hua-Fen Hsu − *Department of Chemistry, National Cheng Kung University, Tainan 701, Taiwan;* orcid.org/0000-0001-8021-193X; Email: konopka@mail.ncku.edu.tw

Shengfa Ye − *State Key Laboratory of Catalysis, Dalian Institute of Chemical Physics, Chinese Academy of Sciences, Dalian 116023, P. R. China; Max-Planck-Institut für Kohlenforschung, Mülheim an der Ruhr D-45470, Germany;* orcid.org/0000-0001-9747-1412; Email: shengfa.ye@dicp.ac.cn

Authors

Hung-Ruei Pan − *Department of Chemistry, National Cheng Kung University, Tainan 701, Taiwan;* orcid.org/0000-0002-1952-3384

Hsin-Jou Chen − *Department of Chemistry, National Cheng Kung University, Tainan 701, Taiwan*

https://doi.org/10.1021/jacsau.1c00184
JACS Au 2021, 1, 1389−1398

Zong-Han Wu − *Department of Chemistry, National Cheng Kung University, Tainan 701, Taiwan*
Pu Ge − *School of Environmental Science and Technology, Dalian University of Technology, Dalian 116024, P. R. China*
Gene-Hsiang Lee − *Department of Chemistry, National Taiwan University, Taipei 106, Taiwan*

Complete contact information is available at: https://pubs.acs.org/10.1021/jacsau.1c00184

Notes

The authors declare no competing financial interest.

■ ACKNOWLEDGMENTS

We thank Ms. Shu-Yi Sun, Mr. Tsung-Lun Kan, and Mr. Bo-Rong Su at Instrument Center of National Cheng Kung University for assisting the measurements of elemental analysis, NMR, and ESI-MS, respectively. We thank the Ministry of Science and Technology in Taiwan for financial support (MOST 109-2113-M-006-007). H.-R.P. gratefully acknowledges the Ph.D. fellowship from Science College of National Cheng Kung University and Ministry of Science and Technology in Taiwan. S.Y. gratefully acknowledges the financial support from the Max-Planck Society, in particular, the joint work space of MPI-CEC and MPI-KOFO. G.P. gratefully acknowledges the financial support from the National Natural Science Foundation of China (No. 22006008).

■ REFERENCES

(1) Huang, X.; Groves, J. T. Oxygen Activation and Radical Transformations in Heme Proteins and Metalloporphyrins. *Chem. Rev.* **2018**, *118* (5), 2491−2553.
(2) Elwell, C. E.; Gagnon, N. L.; Neisen, B. D.; Dhar, D.; Spaeth, A. D.; Yee, G. M.; Tolman, W. B. Copper−Oxygen Complexes Revisited: Structures, Spectroscopy, and Reactivity. *Chem. Rev.* **2017**, *117* (3), 2059−2107.
(3) Nam, W. Dioxygen Activation by Metalloenzymes and Models. *Acc. Chem. Res.* **2007**, *40* (7), 465−465.
(4) Jasniewski, A. J.; Que, L. Dioxygen Activation by Nonheme Diiron Enzymes: Diverse Dioxygen Adducts, High-Valent Intermediates, and Related Model Complexes. *Chem. Rev.* **2018**, *118* (5), 2554−2592.
(5) Valentine, J. S. The Dioxygen Ligand in Mononuclear Group VIII Transition Metal Complexes. *Chem. Rev.* **1973**, *73* (3), 235−245.
(6) Vaska, L. Dioxygen-Metal Complexes: Toward a Unified View. *Acc. Chem. Res.* **1976**, *9* (5), 175−183.
(7) Prigge, S. T.; Eipper, B. A.; Mains, R. E.; Amzel, L. M. Dioxygen Binds End-On to Mononuclear Copper in a Precatalytic Enzyme Complex. *Science* **2004**, *304* (5672), 864.
(8) Kovaleva, E. G.; Lipscomb, J. D. Crystal Structures of Fe^{2+} Dioxygenase Superoxo, Alkylperoxo, and Bound Product Intermediates. *Science* **2007**, *316* (5823), 453.
(9) Jeoung, J.-H.; Bommer, M.; Lin, T.-Y.; Dobbek, H. Visualizing the substrate-, superoxo-, alkylperoxo-, and product-bound states at the nonheme Fe(II) site of homogentisate dioxygenase. *Proc. Natl. Acad. Sci. U. S. A.* **2013**, *110* (31), 12625.
(10) Wang, Y.; Liu, K. F.; Yang, Y.; Davis, I.; Liu, A. Observing 3-hydroxyanthranilate-3,4-dioxygenase in action through a crystalline lens. *Proc. Natl. Acad. Sci. U. S. A.* **2020**, *117* (33), 19720.
(11) Schlichting, I.; Berendzen, J.; Chu, K.; Stock, A. M.; Maves, S. A.; Benson, D. E.; Sweet, R. M.; Ringe, D.; Petsko, G. A.; Sligar, S. G. The Catalytic Pathway of Cytochrome P450cam at Atomic Resolution. *Science* **2000**, *287* (5458), 1615.
(12) Karlsson, A.; Parales, J. V.; Parales, R. E.; Gibson, D. T.; Eklund, H.; Ramaswamy, S. Crystal Structure of Naphthalene Dioxygenase: Side-on Binding of Dioxygen to Iron. *Science* **2003**, *299* (5609), 1039.
(13) Jeoung, J.-H.; Nianios, D.; Fetzner, S.; Dobbek, H. Quercetin 2,4-Dioxygenase Activates Dioxygen in a Side-On O_2−Ni Complex. *Angew. Chem., Int. Ed.* **2016**, *55* (10), 3281−3284.
(14) Cramer, C. J.; Tolman, W. B.; Theopold, K. H.; Rheingold, A. L. Variable character of O-O and M-O bonding in side-on (η^2) 1:1 metal complexes of O_2. *Proc. Natl. Acad. Sci. U. S. A.* **2003**, *100* (7), 3635−3640.
(15) Cho, J.; Woo, J.; Nam, W. An "End-On" Chromium(III)-Superoxo Complex: Crystallographic and Spectroscopic Characterization and Reactivity in C-H Bond Activation of Hydrocarbons. *J. Am. Chem. Soc.* **2010**, *132* (17), 5958−5959.
(16) Hong, S.; Sutherlin, K. D.; Park, J.; Kwon, E.; Siegler, M. A.; Solomon, E. I.; Nam, W. Crystallographic and spectroscopic characterization and reactivities of a mononuclear non-haem iron-(III)-superoxo complex. *Nat. Commun.* **2014**, *5*, 5440.
(17) Iovan, D. A.; Wrobel, A. T.; McClelland, A. A.; Scharf, A. B.; Edouard, G. A.; Betley, T. A. Reactivity of a stable copper−dioxygen complex. *Chem. Commun.* **2017**, *53* (74), 10306−10309.
(18) Oddon, F.; Chiba, Y.; Nakazawa, J.; Ohta, T.; Ogura, T.; Hikichi, S. Characterization of Mononuclear Non-heme Iron (III)-Superoxo Complex with a Five-Azole Ligand Set. *Angew. Chem., Int. Ed.* **2015**, *54* (25), 7336−7339.
(19) Qin, K.; Incarvito, C. D.; Rheingold, A. L.; Theopold, K. H. A Structurally Characterized Chromium(III) Superoxide Complex Features "Side-on" Bonding. *Angew. Chem., Int. Ed.* **2002**, *41* (13), 2333−2335.
(20) Würtele, C.; Gaoutchenova, E.; Harms, K.; Holthausen, M. C.; Sundermeyer, J.; Schindler, S. Crystallographic Characterization of a Synthetic 1:1 End-On Copper Dioxygen Adduct Complex. *Angew. Chem., Int. Ed.* **2006**, *45* (23), 3867−3869.
(21) Yao, S.; Bill, E.; Milsmann, C.; Wieghardt, K.; Driess, M. A "Side-on" Superoxonickel Complex [LNi(O_2)] with a Square-Planar Tetracoordinate Nickel(II) Center and Its Conversion into [LNi(μ-OH)$_2$NiL]. *Angew. Chem., Int. Ed.* **2008**, *47* (37), 7110−7113.
(22) Aboelella, N. W.; Kryatov, S. V.; Gherman, B. F.; Brennessel, W. W.; Young, V. G.; Sarangi, R.; Rybak-Akimova, E. V.; Hodgson, K. O.; Hedman, B.; Solomon, E. I.; Cramer, C. J.; Tolman, W. B. Dioxygen Activation at a Single Copper Site: Structure, Bonding, and Mechanism of Formation of 1:1 Cu-O_2 Adducts. *J. Am. Chem. Soc.* **2004**, *126* (51), 16896−16911.
(23) Aboelella, N. W.; Lewis, E. A.; Reynolds, A. M.; Brennessel, W. W.; Cramer, C. J.; Tolman, W. B. Snapshots of Dioxygen Activation by Copper: The Structure of a 1:1 Cu/O_2 Adduct and Its Use in Syntheses of Asymmetric Bis(μ-oxo) Complexes. *J. Am. Chem. Soc.* **2002**, *124* (36), 10660−10661.
(24) Annaraj, J.; Cho, J.; Lee, Y.-M.; Kim, S. Y.; Latifi, R.; de Visser, S. P.; Nam, W. Structural Characterization and Remarkable Axial Ligand Effect on the Nucleophilic Reactivity of a Nonheme Manganese(III)−Peroxo Complex. *Angew. Chem., Int. Ed.* **2009**, *48* (23), 4150−4153.
(25) Cho, J.; Jeon, S.; Wilson, S. A.; Liu, L. V.; Kang, E. A.; Braymer, J. J.; Lim, M. H.; Hedman, B.; Hodgson, K. O.; Valentine, J. S.; Solomon, E. I.; Nam, W. Structure and reactivity of a mononuclear non-haem iron(III)−peroxo complex. *Nature* **2011**, *478* (7370), 502−505.
(26) Cho, J.; Kang, H. Y.; Liu, L. V.; Sarangi, R.; Solomon, E. I.; Nam, W. Mononuclear nickel(ii)-superoxo and nickel(iii)-peroxo complexes bearing a common macrocyclic TMC ligand. *Chem. Sci.* **2013**, *4* (4), 1502−1508.
(27) Cho, J.; Sarangi, R.; Annaraj, J.; Kim, S. Y.; Kubo, M.; Ogura, T.; Solomon, E. I.; Nam, W. Geometric and electronic structure and reactivity of a mononuclear 'side-on' nickel(iii)−peroxo complex. *Nat. Chem.* **2009**, *1* (7), 568−572.
(28) Cho, J.; Sarangi, R.; Kang, H. Y.; Lee, J. Y.; Kubo, M.; Ogura, T.; Solomon, E. I.; Nam, W. Synthesis, Structural, and Spectroscopic

Characterization and Reactivities of Mononuclear Cobalt(III)-Peroxo Complexes. *J. Am. Chem. Soc.* **2010**, *132* (47), 16977−16986.
(29) Colmer, H. E.; Geiger, R. A.; Leto, D. F.; Wijeratne, G. B.; Day, V. W.; Jackson, T. A. Geometric and electronic structure of a peroxomanganese(iii) complex supported by a scorpionate ligand. *Dalton Trans.* **2014**, *43* (48), 17949−17963.
(30) Crump, D. B.; Stepaniak, R. F.; Payne, N. C. Charge distribution in dioxygen complexes of cobalt(III). The crystal structure and absolute configuration of (+)546-Δ-*cis*-β-[{2,13-dimethyl-6,9-diphenyl-2,6,9,13-tetraarsatetradecane}(dioxygen)-cobalt(III)] perchlorate. *Can. J. Chem.* **1977**, *55* (3), 438−446.
(31) de Sousa, D. P.; Bigelow, J. O.; Sundberg, J.; Que, L.; McKenzie, C. J. Caught! Crystal trapping of a side-on peroxo bound to Cr(iv). *Chem. Commun.* **2015**, *51* (14), 2802−2805.
(32) DeRosha, D. E.; Mercado, B. Q.; Lukat-Rodgers, G.; Rodgers, K. R.; Holland, P. L. Enhancement of C-H Oxidizing Ability in Co−O_2 Complexes through an Isolated Heterobimetallic Oxo Intermediate. *Angew. Chem., Int. Ed.* **2017**, *56* (12), 3211−3215.
(33) Halpern, J.; Goodall, B. L.; Khare, G. P.; Lim, H. S.; Pluth, J. J. Reaction of oxygen with dicyanotris(dimethylphenylphosphine)-cobalt(II). Synthesis, structure, and reactivity of a novel cobalt-dioxygen adduct. *J. Am. Chem. Soc.* **1975**, *97* (8), 2301−2303.
(34) House, D. A.; Garner, C. S. Diperoxodiethylenetriamminechromium(IV) 1-hydrate: a New Chromium(IV) Peroxo Compound. *Nature* **1965**, *208* (5012), 776−777.
(35) Hu, X.; Castro-Rodriguez, I.; Meyer, K. Dioxygen Activation by a Low-Valent Cobalt Complex Employing a Flexible Tripodal N-Heterocyclic Carbene Ligand. *J. Am. Chem. Soc.* **2004**, *126* (41), 13464−13473.
(36) Kang, H.; Cho, J.; Cho, K.-B.; Nomura, T.; Ogura, T.; Nam, W. Mononuclear Manganese−Peroxo and Bis(μ-oxo)dimanganese Complexes Bearing a Common N-Methylated Macrocyclic Ligand. *Chem. - Eur. J.* **2013**, *19* (42), 14119−14125.
(37) Kim, J.; Shin, B.; Kim, H.; Lee, J.; Kang, J.; Yanagisawa, S.; Ogura, T.; Masuda, H.; Ozawa, T.; Cho, J. Steric Effect on the Nucleophilic Reactivity of Nickel(III) Peroxo Complexes. *Inorg. Chem.* **2015**, *54* (13), 6176−6183.
(38) Kishima, T.; Matsumoto, T.; Nakai, H.; Hayami, S.; Ohta, T.; Ogo, S. A High-Valent Iron(IV) Peroxo Core Derived from O_2. *Angew. Chem., Int. Ed.* **2016**, *55* (2), 724−727.
(39) Kitajima, N.; Komatsuzaki, H.; Hikichi, S.; Osawa, M.; Moro-Oka, Y. A Monomeric Side-On Peroxo Manganese(III) Complex: $Mn(O_2)(3,5\text{-}^{i}Pr_2pzH)(HB(3,5\text{-}^{i}Pr_2pz)_3)$. *J. Am. Chem. Soc.* **1994**, *116* (25), 11596−11597.
(40) Lee, C.-M.; Chuo, C.-H.; Chen, C.-H.; Hu, C.-C.; Chiang, M.-H.; Tseng, Y.-J.; Hu, C.-H.; Lee, G.-H. Structural and Spectroscopic Characterization of a Monomeric Side-On Manganese(IV) Peroxo Complex. *Angew. Chem., Int. Ed.* **2012**, *51* (22), 5427−5430.
(41) Noh, H.; Jeong, D.; Ohta, T.; Ogura, T.; Valentine, J. S.; Cho, J. Distinct Reactivity of a Mononuclear Peroxocobalt(III) Species toward Activation of Nitriles. *J. Am. Chem. Soc.* **2017**, *139* (32), 10960−10963.
(42) Rahman, A. F. M. M.; Jackson, W. G.; Willis, A. C. The First Sideways-Bonded Peroxo Complex for a Tetraaminecobalt(III) Species. *Inorg. Chem.* **2004**, *43* (24), 7558−7560.
(43) Ramsey, C. M.; Cage, B.; Nguyen, P.; Abboud, K. A.; Dalal, N. S. Ligand Dependence of Magnetic Dimensionality in Chromium(IV) Complexes: Layered vs Three-Dimensional Antiferromagnets. *Chem. Mater.* **2003**, *15* (1), 92−99.
(44) Reynolds, A. M.; Gherman, B. F.; Cramer, C. J.; Tolman, W. B. Characterization of a 1:1 Cu-O2 Adduct Supported by an Anilido Imine Ligand. *Inorg. Chem.* **2005**, *44* (20), 6989−6997.
(45) Schaefer, W. P.; Huie, B. T.; Kurilla, M. G.; Ealick, S. E. Oxygen-carrying cobalt complexes. 10. Structures of N, N'-ethylenebis(3-tert-butylsalicylideniminato)cobalt (II) and its monomeric dioxygen adduct. *Inorg. Chem.* **1980**, *19* (2), 340−344.
(46) Seo, M. S.; Kim, J. Y.; Annaraj, J.; Kim, Y.; Lee, Y.-M.; Kim, S.-J.; Kim, J.; Nam, W. $[Mn(tmc)(O_2)]^+$: A Side-On Peroxido Manganese(III) Complex Bearing a Non-Heme Ligand. *Angew. Chem., Int. Ed.* **2007**, *46* (3), 377−380.
(47) Singh, U. P.; Sharma, A. K.; Hikichi, S.; Komatsuzaki, H.; Moro-Oka, Y.; Akita, M. Hydrogen bonding interaction between imidazolyl N−H group and peroxide: Stabilization of Mn(III)-peroxo complex $Tp^{iPr2}Mn(\eta^2\text{-}O_2)(im^{Me}H)$ ($im^{Me}H$ = 2-methylimidazole). *Inorg. Chim. Acta* **2006**, *359* (13), 4407−4411.
(48) Terry, N. W.; Amma, E. L.; Vaska, L. Molecular oxygen binding in a monomeric cobalt complex. Crystal and molecular structure of dioxygen-bis[*cis*-1,2-bis(diphenylphosphino)ethylene]cobalt tetrafluoroborate. *J. Am. Chem. Soc.* **1972**, *94* (2), 653−655.
(49) VanAtta, R. B.; Strouse, C. E.; Hanson, L. K.; Valentine, J. S. Peroxo(tetraphenylporphinato)manganese(III) and chloro(tetraphenylporphinato)manganese(II) anions. Synthesis, crystal structures, and electronic structures. *J. Am. Chem. Soc.* **1987**, *109* (5), 1425−1434.
(50) Yokoyama, A.; Han, J. E.; Cho, J.; Kubo, M.; Ogura, T.; Siegler, M. A.; Karlin, K. D.; Nam, W. Chromium(IV)−Peroxo Complex Formation and Its Nitric Oxide Dioxygenase Reactivity. *J. Am. Chem. Soc.* **2012**, *134* (37), 15269−15272.
(51) Zhang, Q.; Bell-Taylor, A.; Bronston, F. M.; Gorden, J. D.; Goldsmith, C. R. Aldehyde Deformylation and Catalytic C−H Activation Resulting from a Shared Cobalt(II) Precursor. *Inorg. Chem.* **2017**, *56* (2), 773−782.
(52) Tomson, N. C.; Williams, K. D.; Dai, X.; Sproules, S.; DeBeer, S.; Warren, T. H.; Wieghardt, K. Re-evaluating the Cu K pre-edge XAS transition in complexes with covalent metal−ligand interactions. *Chem. Sci.* **2015**, *6* (4), 2474−2487.
(53) Chang, Y.-H.; Chan, P.-M.; Tsai, Y.-F.; Lee, G.-H.; Hsu, H.-F. Catalytic Reduction of Hydrazine to Ammonia by a Mononuclear Iron(II) Complex on a Tris(thiolato)phosphine Platform. *Inorg. Chem.* **2014**, *53* (2), 664−666.
(54) Momenteau, M.; Reed, C. A. Synthetic Heme-Dioxygen Complexes. *Chem. Rev.* **1994**, *94* (3), 659−698.
(55) Shan, X.; Que, L. Intermediates in the oxygenation of a nonheme diiron(II) complex, including the first evidence for a bound superoxo species. *Proc. Natl. Acad. Sci. U. S. A.* **2005**, *102* (15), 5340.
(56) Zhao, M.; Helms, B.; Slonkina, E.; Friedle, S.; Lee, D.; DuBois, J.; Hedman, B.; Hodgson, K. O.; Fréchet, J. M. J.; Lippard, S. J. Iron Complexes of Dendrimer-Appended Carboxylates for Activating Dioxygen and Oxidizing Hydrocarbons. *J. Am. Chem. Soc.* **2008**, *130* (13), 4352−4363.
(57) Chiang, C.-W.; Kleespies, S. T.; Stout, H. D.; Meier, K. K.; Li, P.-Y.; Bominaar, E. L.; Que Jr, L.; Münck, E.; Lee, W.-Z. Characterization of a Paramagnetic Mononuclear Nonheme Iron-Superoxo Complex. *J. Am. Chem. Soc.* **2014**, *136* (31), 10846−10849.
(58) Fischer, A. A.; Lindeman, S. V.; Fiedler, A. T. A synthetic model of the nonheme iron−superoxo intermediate of cysteine dioxygenase. *Chem. Commun.* **2018**, *54* (80), 11344−11347.
(59) Blakely, M. N.; Dedushko, M. A.; Yan Poon, P. C.; Villar-Acevedo, G.; Kovacs, J. A. Formation of a Reactive, Alkyl Thiolate-Ligated Fe^{III}-Superoxo Intermediate Derived from Dioxygen. *J. Am. Chem. Soc.* **2019**, *141* (5), 1867−1870.
(60) Kim, H.; Rogler, P. J.; Sharma, S. K.; Schaefer, A. W.; Solomon, E. I.; Karlin, K. D. Heme-Fe^{III} Superoxide, Peroxide and Hydroperoxide Thermodynamic Relationships: $Fe^{III}\text{-}O_2^{\bullet-}$ Complex H-Atom Abstraction Reactivity. *J. Am. Chem. Soc.* **2020**, *142* (6), 3104−3116.
(61) Chang, K.-C.; Huang, C.-J.; Chang, Y.-H.; Wu, Z.-H.; Kuo, T.-S.; Hsu, H.-F. Reactivity of a Fe(III)-Bound Methoxide Supported with a Tris(thiolato)phosphine Ligand: Activation of C-Cl Bond in CH_2Cl_2 by Nucleophilic Attack of a Fe(III)-OCH_3 Moiety. *Inorg. Chem.* **2016**, *55* (2), 566−572.
(62) Desiraju, G. R. The C-H O Hydrogen Bond in Crystals: What Is It? *Acc. Chem. Res.* **1991**, *24* (10), 290−296.
(63) Holland, P. L. Metal−dioxygen and metal−dinitrogen complexes: where are the electrons? *Dalton Trans.* **2010**, *39* (23), 5415−5425.

https://doi.org/10.1021/jacsau.1c00184
JACS Au 2021, 1, 1389−1398

(64) Kaupp, M.; Danovich, D.; Shaik, S. Chemistry is about energy and its changes: A critique of bond-length/bond-strength correlations. *Coord. Chem. Rev.* **2017**, *344*, 355−362.
(65) Lin, Y.-H.; Kutin, Y.; van Gastel, M.; Bill, E.; Schnegg, A.; Ye, S.; Lee, W.-Z. A Manganese(IV)-Hydroperoxo Intermediate Generated by Protonation of the Corresponding Manganese(III)-Superoxo Complex. *J. Am. Chem. Soc.* **2020**, *142* (23), 10255−10260.
(66) Lin, Y.-H.; Cramer, H. H.; van Gastel, M.; Tsai, Y.-H.; Chu, C.-Y.; Kuo, T.-S.; Lee, I. R.; Ye, S.; Bill, E.; Lee, W.-Z. Mononuclear Manganese(III) Superoxo Complexes: Synthesis, Characterization, and Reactivity. *Inorg. Chem.* **2019**, *58* (15), 9756−9765.
(67) Mondal, B.; Neese, F.; Bill, E.; Ye, S. Electronic Structure Contributions of Non-Heme Oxo-Iron(V) Complexes to the Reactivity. *J. Am. Chem. Soc.* **2018**, *140* (30), 9531−9544.
(68) Herebian, D.; Wieghardt, K. E.; Neese, F. Analysis and Interpretation of Metal-Radical Coupling in a Series of Square Planar Nickel Complexes: Correlated Ab Initio and Density Functional Investigation of [Ni(LISQ)2] (LISQ = 3,5-di-tert-butyl-o-diiminobenzosemiquinonate(1-)). *J. Am. Chem. Soc.* **2003**, *125* (36), 10997−11005.
(69) Jo, Y.; Annaraj, J.; Seo, M. S.; Lee, Y.-M.; Kim, S. Y.; Cho, J.; Nam, W. Reactivity of a cobalt(III)-peroxo complex in oxidative nucleophilic reactions. *J. Inorg. Biochem.* **2008**, *102* (12), 2155−2159.
(70) Block, E.; Ofori-Okai, G.; Zubieta, J. 2-Phosphino- and 2-Phosphinylbenzenethiols: New Ligand Types. *J. Am. Chem. Soc.* **1989**, *111* (6), 2327−2329.
(71) Niemoth-Anderson, J. D.; Clark, K. A.; George, T. A.; Ross, C. R. Five-Coordinate Diamagnetic Iron(IV) Complexes With A Trigonal Planar Arrangement of Thiolate Ligand Atoms: Synthesis and Crystal Structure of [FeX(PS_3)] (X = Cl, Br or I; PS_3H_3 = [P(C‴$_6H_3$-3-Me_3Si-2-SH)$_3$]). *J. Am. Chem. Soc.* **2000**, *122* (16), 3977−3978.
(72) Sheldrick, G. M. *SADABS*; University of Göttingen: Germany, 1996.
(73) Sheldrick, G. *SHELXTL*, version 5; Siemens Analytical Xray Systems. Inc.: Madison, WI, 1994.
(74) van der Vlugt, J. I.; Hewat, A. C.; Neto, S.; Sablong, R.; Mills, A. M.; Lutz, M.; Spek, A. L.; Müller, C.; Vogt, D. Sterically Demanding Diphosphonite Ligands − Synthesis and Application in Nickel-Catalyzed Isomerization of 2-Methyl-3-Butenenitrile. *Adv. Synth. Catal.* **2004**, *346* (8), 993−1003.
(75) Perdew, J. P.; Burke, K.; Ernzerhof, M. Generalized Gradient Approximation Made Simple. *Phys. Rev. Lett.* **1996**, *77* (18), 3865−3868.
(76) Lee, C.; Yang, W.; Parr, R. G. Development of the Colle-Salvetti correlation-energy formula into a functional of the electron density. *Phys. Rev. B: Condens. Matter Mater. Phys.* **1988**, *37* (2), 785−789.
(77) Becke, A. D. Density-functional thermochemistry. III. The role of exact exchange. *J. Chem. Phys.* **1993**, *98* (7), 5648−5652.
(78) Eichkorn, K.; Treutler, O.; Öhm, H.; Häser, M.; Ahlrichs, R. Auxiliary basis sets to approximate Coulomb potentials (Chem. Phys. Letters 240 (1995) 283−290). *Chem. Phys. Lett.* **1995**, *242* (6), 652−660.
(79) Neese, F.; Wennmohs, F.; Hansen, A.; Becker, U. Efficient, approximate and parallel Hartree−Fock and hybrid DFT calculations. A 'chain-of-spheres' algorithm for the Hartree−Fock exchange. *Chem. Phys.* **2009**, *356* (1), 98−109.
(80) Weigend, F.; Ahlrichs, R. Balanced basis sets of split valence, triple zeta valence and quadruple zeta valence quality for H to Rn: Design and assessment of accuracy. *Phys. Chem. Chem. Phys.* **2005**, *7* (18), 3297−3305.
(81) Weigend, F. Accurate Coulomb-fitting basis sets for H to Rn. *Phys. Chem. Chem. Phys.* **2006**, *8* (9), 1057−1065.
(82) Neese, F. Prediction and interpretation of the ^{57}Fe isomer shift in Mössbauer spectra by density functional theory. *Inorg. Chim. Acta* **2002**, *337*, 181−192.
(83) Schäfer, A.; Huber, C.; Ahlrichs, R. Fully optimized contracted Gaussian basis sets of triple zeta valence quality for atoms Li to Kr. *J. Chem. Phys.* **1994**, *100* (8), 5829−5835.
(84) Schäfer, A.; Horn, H.; Ahlrichs, R. Fully optimized contracted Gaussian basis sets for atoms Li to Kr. *J. Chem. Phys.* **1992**, *97* (4), 2571−2577.
(85) Römelt, M.; Ye, S.; Neese, F. Calibration of Modern Density Functional Theory Methods for the Prediction of 57Fe Mössbauer Isomer Shifts: Meta-GGA and Double-Hybrid Functionals. *Inorg. Chem.* **2009**, *48* (3), 784−785.
(86) Ye, S.; Bill, E.; Neese, F. Electronic Structures of the [Fe(N2)(SiPiPr3)]+1/0/−1 Electron Transfer Series: A Counter-intuitive Correlation between Isomer Shifts and Oxidation States. *Inorg. Chem.* **2016**, *55* (7), 3468−3474.
(87) Sinnecker, S.; Slep, L. D.; Bill, E.; Neese, F. Performance of Nonrelativistic and Quasi-Relativistic Hybrid DFT for the Prediction of Electric and Magnetic Hyperfine Parameters in 57Fe Mössbauer Spectra. *Inorg. Chem.* **2005**, *44* (7), 2245−2254.
(88) Neese, F. The ORCA program system. *Wiley Interdiscip. Rev.: Comput. Mol. Sci.* **2012**, *2* (1), 73−78.

https://doi.org/10.1021/jacsau.1c00184
JACS Au 2021, 1, 1389−1398